

## Full Length Article

# Understanding carbide evolution and surface chemistry during deep cryogenic treatment in high-alloyed ferrous alloy

Patricia Jovičević-Klug<sup>a,b,\*</sup>, Levi Tegg<sup>c,d</sup>, Matic Jovičević-Klug<sup>b</sup>, Rahul Parmar<sup>e</sup>, Matteo Amati<sup>e</sup>, Luca Gregoratti<sup>e</sup>, László Almásy<sup>f</sup>, Julie M. Cairney<sup>c,d</sup>, Bojan Podgornik<sup>a</sup>

<sup>a</sup> Institute of Metals and Technology, Lepi pot 11, 1000 Ljubljana, Slovenia

<sup>b</sup> Max-Planck Institute for Iron Research, Max-Planck-Str. 1, 40237 Düsseldorf, Germany

<sup>c</sup> School of Aerospace, Mechanical and Mechatronic Engineering, The University of Sydney, Camperdown, NSW 2006, Australia

<sup>d</sup> Australian Centre for Microscopy and Microanalysis, The University of Sydney, Camperdown, NSW 2006, Australia

<sup>e</sup> Elettra - Sincrotrone Trieste, S.C.p.A., SS14 – km 163.5 in Area Science Park, 34149 Trieste, Italy

<sup>f</sup> Institute for Energy Security and Environmental Safety, Centre for Energy Research, Konkoly-Thege Miklos út. 29-33, 1121 Budapest, Hungary



## ARTICLE INFO

## Keywords:

Cryogenic temperature

Surface chemistry

Microstructure

Atom probe tomography (APT)

Scanning photoelectron microscopy (SPEM)

Small angle neutron scattering (SANS)

## ABSTRACT

The study investigates the effect of deep cryogenic treatment (DCT) on a high-alloyed ferrous alloy (HAFA) and its effectiveness on carbide evolution and chemical shifts of alloying elements. With ex-situ and in-situ observations ranging from the microscopic to the nanoscopic level, we uncover the atomistic mechanism by which DCT affects carbide precipitation, resulting in a 50% increase in carbide volume fraction. Synchrotron-based scanning photoelectron microscopy provides insight into the agglomeration of carbon during exposure to DCT. We find that Mo plays a crucial role in DCT through its modification of chemical bonding states, which is postulated to originate from the loosely-formed primordial  $\text{Mo}_2\text{C}$  carbides formed during exposure to cryogenic temperatures. These in turn provide energetically favorable nucleation zones that accelerate the formation of  $\text{M}_7\text{C}_3$  carbides, which serve as intermediate states for the formation of  $\text{M}_{23}\text{C}_6$  carbides, which most strongly impact the mechanical properties. These results are supported by atom probe tomography, showing the preferential formation of Mo-rich  $\text{M}_7\text{C}_3$  carbides in DCT samples, resulting from greater solute mobility. This work clarifies the fundamental mechanisms on how DCT affects HAFA, solving a long-elusive problem.

## 1. Introduction

Deep cryogenic treatment (DCT) is a type of heat treatment [1,2] or heat treatment technology [3] that has recently become popular due to its cost-effectiveness [4], simple application [5] and positive effect on surface and bulk materials properties. It can be applied to both ferrous and non-ferrous alloys, and can affect properties such as hardness, toughness, corrosion and wear resistance, prolonged material life, and magnetic properties, amongst others [1,2,6–10]. DCT procedures are thus important for many technologies and industries, such as medicine [11,12], robotics [13], materials science [14,15], the fuel and energy sectors [7], electronics [16], the aerospace, tool and steel industries [3,17,18], musical instruments [19] and automotive industry [7]. The changes in the material properties result from the chemical and physical changes in the microstructure during DCT and subsequent tempering (heating of material to induce carbide precipitation). The

microstructural changes following DCT are (1) increased formation and precipitation of finer carbides [6], sometimes described as  $\epsilon$ -carbides and  $\eta$ -carbides [6,20,21], (2) a more homogenous microstructure [20,22–25], (3) transformation of retained austenite into martensite [23,26,27], (4) formation of finer martensitic laths [28,29], (5) orientation of newly formed martensitic laths in the [101] and [001] directions [28], and (6) different oxidation dynamics on the surface [28,30]. However, despite intensive experimental and some theoretical research in the last decade, the underlying mechanisms for the strong effect of DCT remains unclear.

Several theories have been proposed to describe how DCT affects the microstructure and material properties. Jaswin and Mohan Lal (2015) [23] and Kumar et al. (2016) [31] postulated that DCT increases the driving force for the carbide nucleation through lattice energy reduction, and finer martensite formation from transforming retained austenite, which together result in increased precipitation and finer

\* Corresponding author at: Max-Planck Institute for Iron Research, Max-Planck-Str. 1, 40237 Düsseldorf, Germany.

E-mail addresses: [p.jovicevic-klug@mpie.de](mailto:p.jovicevic-klug@mpie.de), [patricia.jovicevicklug@imt.si](mailto:patricia.jovicevicklug@imt.si) (P. Jovičević-Klug).

<https://doi.org/10.1016/j.apsusc.2022.155497>

Received 5 August 2022; Received in revised form 15 October 2022; Accepted 25 October 2022

Available online 29 October 2022

0169-4332/© 2022 The Authors. Published by Elsevier B.V. This is an open access article under the CC BY-NC license (<http://creativecommons.org/licenses/by-nc/4.0/>).

carbides. Meng et al. (1994) [20] suggested that another possible mechanism for retirement is the precipitation of  $\eta$ -carbides, instead of  $\varepsilon$ -carbides that normally form during conventional heat treatment. However, Gavriljuk et al. (2013) [22] considers the theory relating to these transiting carbides vague, as their short lifetime and metastability in the initial stage of tempering make them hard to track and analyze. Instead, Gavriljuk et al. (2013) [22] explained that the additional carbide nucleation occurs due to direct plastic deformation of the martensite during exposure to DCT, which results in carbon displacement and agglomeration with gliding dislocations. Another possible mechanism is described by Collins (1996) [32], who stated that DCT influences the production of internal stresses following the austenite to martensite transformation. This effect, as proposed by Moore and Collins (1993) [24], results in martensite conditioning, which promotes formation of fine carbides through additional formation of nucleation sites. They assumed that the additional nucleation sites are activated by recombination and formation of crystal defects or carbon clusters, which form a lower energy potential for preferential carbide nucleation. Furthermore, Collins (1996) [32] suggested that internal stresses may spawn twins and dislocations in crystal lattice defects. Huang et al. (2003) [29] and Antony et al. (2020) [33] suggested that supersaturation of martensite during DCT increases its lattice distortion and thermodynamic instability due to the extremely low temperature, which then promotes the migration of carbon and alloying elements towards nearby crystal defects. Akhbarizadeh et al. (2009) [34] proposed that increased carbide precipitation results from martensite and austenite lattice contraction. As a result of martensitic contraction and conditioning, residual stresses in the material change to become compressive [35].

To date, studies into DCT have been mainly focused on the physical changes related to mechanical properties and have not linked these changes to chemical effects connected with the modified microstructure [6,36–38]. However, the proposed theories related to the stress, saturation and distortion state of the matrix fail to explain the varying effect of DCT on the properties of different highly-alloyed ferrous alloys (HAFAs) [21,36,37,39]. The effects of DCT on microstructure can vary significantly between different HAFAs despite small changes in composition [21,36,37,39]. Furthermore, no theory satisfactorily explains why DCT has no effect on carbide precipitation for certain HAFAs, since the martensite transformation still occurs and should be similarly modified by DCT, while in others a 100 % increase in carbide precipitation was observed [21,36,37,39]. Thus, the current theories are unable to explain the fundamental impacts of DCT on HAFAs, which we speculate to be of chemical origin.

The relationship between surface and bulk properties following DCT has not been thoroughly studied, especially the influence of solute mobility and chemical state on the carbide formation and precipitation. Some studies have suggested that the reduced number of carbide clusters after DCT could be related to oxygen absorption and changes in oxidation state of the metallic matrix [24,28]. Oxygen absorption analysis has shown that DCT leads to refinement of martensitic laths in the matrix, resulting in a smoother surface [28]. Some DCT studies [21,39–44] have investigated the presence of selected alloying elements (Co, Cr and W) in carbides, however no research was done to link this to chemical changes during DCT and their migration in the microstructure. Only with the understanding of the mechanisms behind DCT, and the manipulation of carbides and other microstructural features following DCT, can the enhancements of targeted properties be understood. This would not only confirm our proposed mechanism, but also provide the understanding required for the full utilization of DCT on different metallic materials for different technologies and industries.

In this work, we investigate the correlation between chemical changes induced by DCT and the physical changes and proposed mechanisms in a selected model HAFAs, EN HS6-5-3 (also known as AISI M3:2). The effect of DCT will be compared to a sample which has undergone conventional heat treatment (CHT) without DCT. This has been

performed using correlative microscopy and materials analysis techniques, including scanning-electron microscopy (SEM), transmission-electron microscopy (TEM), atom probe tomography (APT), small angle neutron scattering (SANS) and in-situ scanning photoelectron microscopy (SPEM) at the ESCA microscopy beamline at Elettra synchrotron (Italy) [45]. Our findings reveal the change in the electron binding energies of the alloying elements following DCT, and link those changes to the modified microstructural evolution, particularly nano-scale carbide formation and precipitation. The ex-situ microscopy results and the in-situ SPEM observations deliver a definitive answer and reasoning to the DCT effect on carbide precipitation and the impactful influence of the binding energy state of alloying elements on the proposed mechanism of DCT.

## 2. Methods

### 2.1. Material and heat treatment

Selected material was PM high-alloyed ferrous alloy (HAFAs) EN HS6-5-3 (also known as AISI M3:2), supplied in soft annealed state by producer ERasteel, Hilden, Germany. The chemical composition of HAFAs in wt. %, is 1.29C, 5.90 W, 3.90 Cr, 4.80 Mo, 3.00 V, 0.69 Co, 0.006 S, 0.31 Mn and 80.10 Fe. HAFAs samples were firstly heat-treated to austenitization at 1050 °C for 2 min in horizontal vacuum furnace IPSEN VTTC-324R (Ipsen, Kleve, Germany) with uniform high-pressure gas quenching using N<sub>2</sub> at the pressure of 5 bars (average quenching rate was approximately 7–8 °C / s). After quenching, samples were divided to two groups: first-control, which was conventionally heat-treated (CHT), and second-testing group, which was deep cryogenically heat-treated (DCT). The first CHT group was after quenching exposed to triple tempering (3 × 600 °C for 2 h). Whereas; the second DCT group was subjected to cryogenic temperatures by gradual immersion (10 °C / min) in liquid nitrogen for 24 h (1 day) at –196 °C, which was performed immediately after quenching and followed by only a single tempering cycle (1 × 600 °C for 2 h). Selected heat treatment parameters were chosen based on our previous research of HAFAs [21,28]. In addition, CHT and DCT samples for SEM analysis were etched according to the methods described in Jovičević-Klug et al. 2021 [46].

### 2.2. Microscopy and phase analysis

Microstructural analysis of HAFAs was performed using a scanning electron microscope (SEM) Zeiss Crossbeam 550 FIB-SEM Gemini II (Oberkochen, Germany), and a transmission electron microscope (TEM) JEOL JEM-2100 (Tokyo, Japan) at Institute of Metals and Technology. Phase analysis of HAFAs is based/provided by our previous study [21]. Statistical evaluation of particles was conducted by SPSS, PASWStatistics18, SPSS Inc., (Chicago, IL, USA).

### 2.3. Small angle neutron scattering (SANS)

Small angle neutron scattering (SANS) experiments were carried out using the Yellow Submarine diffractometer at the Budapest Neutron Center [47]. Samples for HAFAs were attached to a sample changer and were measured at room temperature. The range of scattering vectors  $q$  was 0.016 to 0.45 Å<sup>-1</sup>, where  $q = 4 \pi \lambda \sin \theta$  with  $2\theta$  is the scattering angle. In order to access to a broad range of  $q$ , two different configurations were used with sample-detector distances were 1.15 m or 5.125 m with the incident neutron wavelength set to be 4.2 Å. The raw data have been corrected for sample transmission and room background. Correction to the detector efficiency and conversion of the measured scattering to absolute scale was performed by normalizing the spectra to the scattering from a light water sample.

#### 2.4. Atom probe tomography (APT)

Specimens were prepared for atom probe tomography (APT) by electropolishing matchstick sections, first using 25 % perchloric acid in glacial acetic acid with  $\approx 15$  V DC, then using 2 % perchloric acid in 2-butoxyethanol at 5–10 V DC [48]. APT was performed using a Cameca LEAP4000X Si at Sydney Microscopy and Microanalysis, The University of Sydney. Specimens were analyzed at 50 K and evaporated in laser-pulsed mode with 355 nm wavelength, 150 pJ laser pulse energy and 200 kHz repetition rate. The standing voltage was controlled to result in a 2 % detection rate (0.02 ions per pulse), with 57 % detector efficiency. Data reconstruction was performed using AP Suite 6.2 [49]. As no crystallographic poles were observed on the detector and the data collection ended without tip fracture, the radius evolution was calculated from the standing voltage, and the image compression factor and

field factor were estimated using post-analysis SEM images [48]. Analysis of the reconstruction was performed using the IVAS module of AP Suite 6.2. Cluster analysis of carbides was performed using the routines included within AP Suite and considered clusters of C, C<sub>3</sub> and C<sub>4</sub> ions. The maximum separation  $d_{max}$  was chosen as the distance corresponding to the maximum difference between the observed nearest-neighbor distribution and that calculated by randomly assigning ionic identities. The minimum cluster size was set to eliminate the probability of a random cluster being included in the analysis. The erosion and envelope parameters were both set to  $\frac{1}{2}d_{max}$ . Isosurfaces were calculated using a voxel grid with 1 nm spacing and 3 nm of delocalization.

#### 2.5. Scanning photoelectron microscopy (SPEM)

The scanning photoelectron microscopy (SPEM) was performed at

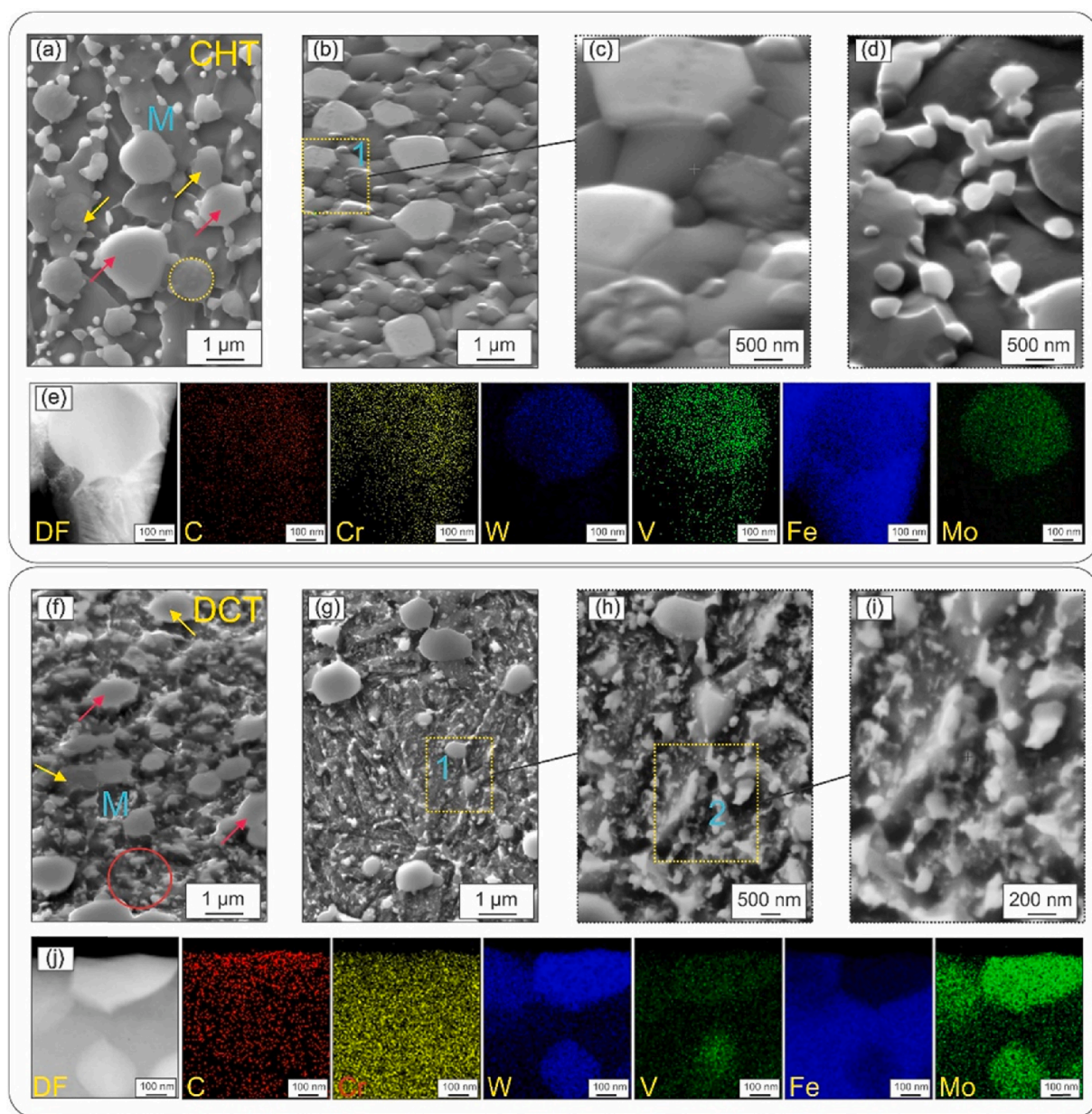


**Fig. 1.** Conventionally heat-treated (CHT) (a-e) and deep cryogenically heat-treated (DCT) (f-j) sample of HAFAs. Micrographs (a-d, f-i) show typical microstructures imaged under SEM, where M represents martensite (matrix) and the colored arrows indicate different types of carbides: yellow arrow is MC enriched by V, and red arrow is M<sub>6</sub>C enriched with Cr, Mo and Fe [21]. Yellow circle in (a) marks the formation of complex bonbon carbides. Red circle in (f) marks the formation of complex M<sub>23</sub>C<sub>6</sub> carbides (c-d and h-i) are enlarged selected regions. Micrographs (e and j) show dark-field STEM and EDS mapping of selected chemical elements for the carbide precipitation interpretation.

the ESCA Microscopy beamline at the Elettra synchrotron radiation center.; The base pressure of the microscope chamber was  $3 \times 10^{-10}$  mbar; and the photon energy of 750 eV. Samples were pre-quenched at the Institute of Metals and Technology, and were then analyzed in-situ during the DCT (24 h) and tempering stages ( $1 \times 550$  °C / 2 h for both samples) for both setups (CHT/DCT). Before the experiments, samples were ion milled with Ar to remove oxide layer and surface contaminants. The cleanliness of each sample was thoroughly checked and no contaminants were found. The surface chemistry of samples was mapped with high spatial resolution and spectral surveys. The chemical surface maps of C1s, Cr2p, Fe3p, Mo3d, V2p and W4f) were recorded at photon energies of 750 eV (Fe-based). For a correct interpretation of the maps a subtraction of the topography signal was also analyzed using existing procedures [45], so that the photoemission intensity maps represented the proper chemical contrast. The analysis of data was conducted by IgorPro8, WaveMetrics (Portland, OR, USA) and Origin, version 2021, OriginLab Corporation (Northampton, MA, USA).

### 3. Results and discussion

#### 3.1. Carbide changes between CHT and DCT

The HAFA consists primarily of a martensite matrix supporting carbides of several different types. The primary carbides are  $M_6C$  and MC,

marked with colored arrows in the SEM micrographs shown in Fig. 1a and Fig. 1f. These carbides are respectively enriched in W and V, and form due to the specific alloying contents of the investigated HAFA and its heat treatment scheme. In addition, sub-micrometer sized carbides also form in the HAFA during the final tempering stage, which are primarily enriched with Cr and Fe. These carbides are strongly affected by the exposure to liquid nitrogen temperatures during DCT. In contrast to the CHT HAFA, the DCT variant displays much higher density of  $M_{23}C_6$  carbides, a smaller average size and a more homogeneous distribution across the martensitic matrix (compare Fig. 1a-d with Fig. 1f-i).

Given the changes to the morphology and distribution of the carbides, the chemical composition must be modified to compensate for the massive changes in their nucleation and growth. These changes can be identified through EDS analysis of the carbides. The Fe-based  $M_{23}C_6$  carbides in the CHT sample display enrichment of the main alloying elements W, Mo and V, but also with Cr (see Fig. 1e). DCT samples also have the  $M_{23}C_6$  carbides observed in the CHT sample as well as an additional subtype, which is considerably more enriched with Cr and V (see Fig. 1j). The two alloying types of the sub-micrometer carbides indicate the slow transition of the  $M_{23}C_6$  carbides to the  $M_6C$  carbides that are the final carbide state after prolonged tempering [21]. However, EDS provides no information about the carbides with diameter below 100 nm, which are present in both CHT and DCT samples (visible in the SEM micrographs of APT tips in S1) [21]. In contrast to the larger sub-

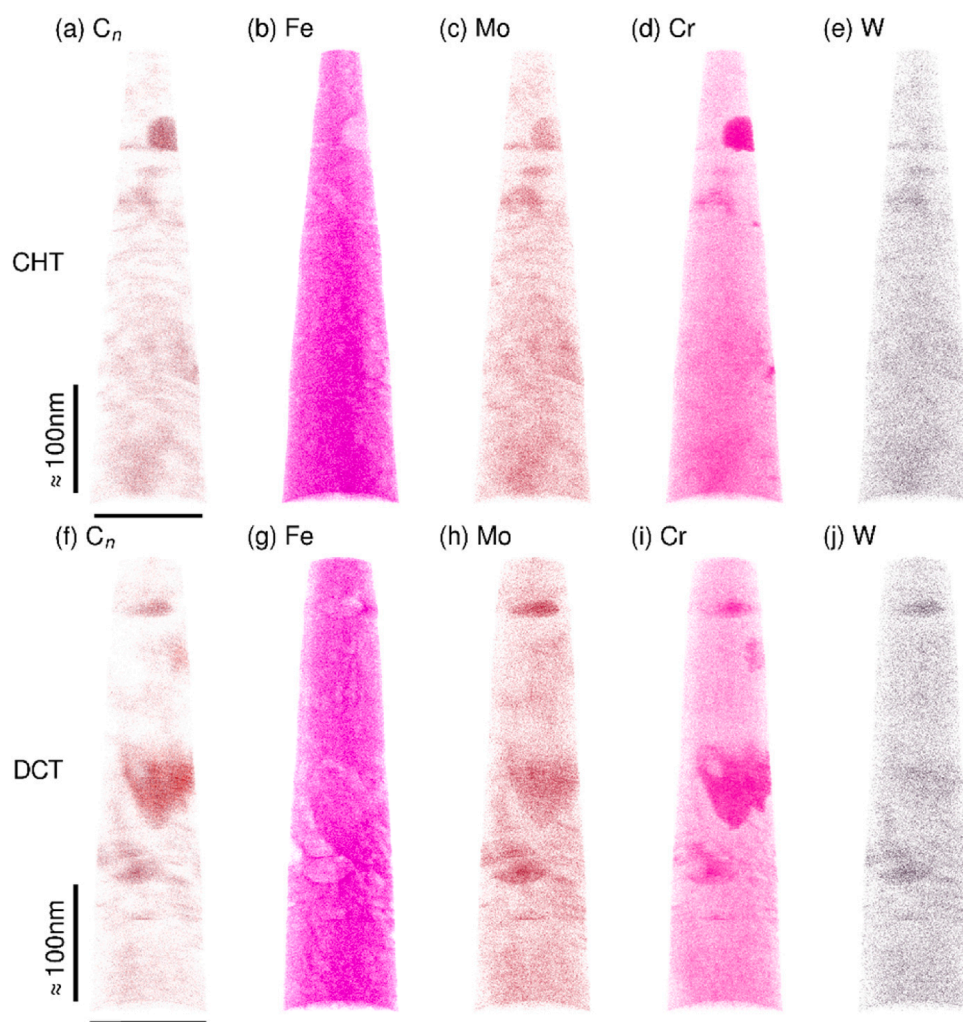


**Fig. 2.** Atom probe reconstructions showing the 3D structure of conventionally heat-treated (CHT) and deep cryogenically heat-treated (DCT) samples of HAFA. The columns show the distributions of alloying elements (a-f) C, (b-g) Fe, (c-h) Mo, (d-i) Cr and (e-j) W the selected testing samples for APT analysis. Note the scale bar is approximate as these datasets were not spatially calibrated.

micrometer  $M_{23}C_6$  carbides, these carbides are more similarly sized and distributed for both CHT and DCT samples.

### 3.2. Atomic scale chemical modifications of carbides with DCT

APT reveals the chemical composition of the nanometer-sized carbides of both CHT and DCT samples. Figs. 2 and S2a (CHT-3D model, Fe and C) show APT reconstructions of the CHT and DCT samples, showing

the reconstructed positions of some important elements. Analysis of the largest C-rich clusters reveals two major types of carbides in both the CHT and DCT samples. The first group is determined to have a higher C and Mo content, corresponding to an  $M_7C_3$  carbide type (Fig. 3a), and the other a higher Fe and Cr content, corresponding to the  $M_{23}C_6$  carbide type (Fig. 3b). C isoconcentration surfaces (isosurfaces) and proximity histograms (proxigrams) show the distribution of alloying elements around the matrix:carbide interface of some large, exemplar carbides.

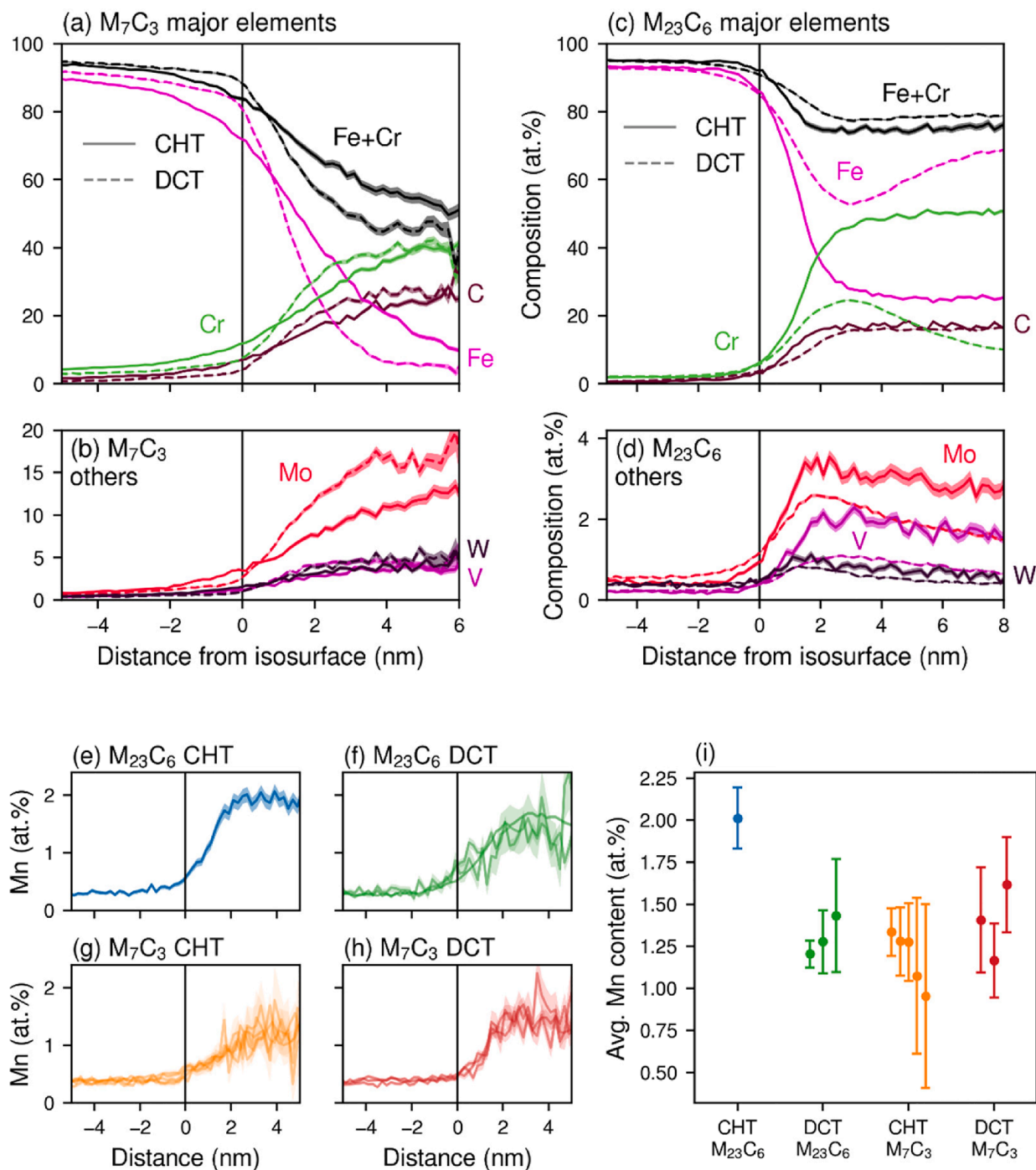


**Fig. 3.** Proximity histograms (proxigrams) of the alloying content around exemplar (a, b)  $M_7C_3$  carbides and (c,d)  $M_{23}C_6$  carbides for both CHT and DCT samples, generated from C isoconcentration surfaces (isosurfaces). Positive distances (right) are inside the carbide, negative distances (left) are in the matrix. For visual clarity, major elements are shown in (a, b), minor elements in (c, d). Solid lines indicate data from the CHT sample, dashed lines from the DCT sample. The shaded region represents the uncertainty in composition at each position. (e-h) Proxigrams displaying Mn distribution for both CHT and DCT samples. Proxigrams from each carbide are visually overlaid to emphasize their similarity. (i) Average Mn contents from the core of each carbide found. The error bars represent the standard deviation. Note that the distance axis in this figure should be considered approximate as these datasets were not spatially calibrated.

Fig. 3a,b and 3c,d show proxigrams around the exemplar  $M_7C_3$  and  $M_{23}C_6$  carbides, for both the CHT and DCT sample. With DCT the Mo content is  $\approx 36\%$  higher for the  $M_7C_3$  carbide and  $\approx 33\%$  lower for the  $M_{23}C_6$  carbide in comparison to the CHT ones. Additionally, the  $M_{23}C_6$  carbides display twice the V content after CHT compared to DCT (Fig. 3b and S2b). These chemical changes indicate that with DCT the  $M_{23}C_6$  carbides preferentially form with higher Fe content and lower content of other alloying elements. Such phenomena are explained by the lower nucleation barrier of the  $M_{23}C_6$  carbides and higher mobility of the alloying elements towards the larger carbides, which consume the heavier alloying elements (Cr, V and Mo) [50]. This is further supported by the Cr and Fe proxigrams, which identify a core-shell structure of DCT carbides with enriched Cr shell. The possibility of diffusion-limited carbide growth due to a different number of tempering cycles of the CHT and DCT can be dismissed due to the similar C and Fe + Cr proxigrams for both CHT and DCT  $M_{23}C_6$  carbides. In contrast, the  $M_7C_3$  carbides show similar chemical structure and proxigram evolution between CHT and DCT samples, with the exception of the Mo increasing in exchange of Fe for DCT. This suggests that DCT induces a preferential formation of secondary  $M_7C_3$  carbide type through the agglomeration of Mo in the initial part of tempering. This is consistent with the thermodynamic modelling, which indicates a separate  $M_7C_3$  carbide formation with the additional exposure of the HAFA to cryogenic temperatures [21].

The phenomenon of increased carbide formation and dealloying of them following DCT is also supported by the Mn content in the carbides. Mn is generally a low-alloying element in carbides [51], so its smaller variations within the carbides give an indication about the affinity towards enrichment of carbides with solute atoms. The distribution of Mn around all of the  $M_{23}C_6$  and  $M_7C_3$  carbides found is shown in Fig. 3e-h. The average Mn contents in the core of the carbides are shown in Fig. 3i. From the proxigrams of all the carbides, the affinity for alloying of  $M_7C_3$  carbides is not altered, whereas for the  $M_{23}C_6$  carbides there is a stronger alloying with Mn for the CHT sample compared to the DCT sample. Furthermore, the Mn content in  $M_{23}C_6$  DCT is similar to the values of the  $M_7C_3$  carbides, which further support the lower alloying affinity with DCT.

The APT results also suggested that the volumetric fraction of nanometer-scale carbides is  $\approx 30\%$  larger for the DCT sample compared to the CHT sample. However, the analysis volume in APT is very small, and cannot represent a statistically valid determination of the nanoscopic particles. Instead, the distribution of these nanometer-scale carbides was studied with SANS which probes centimeter-scale sample volume but with sensitivity to nanometer-scale features. Fig. 4 shows the

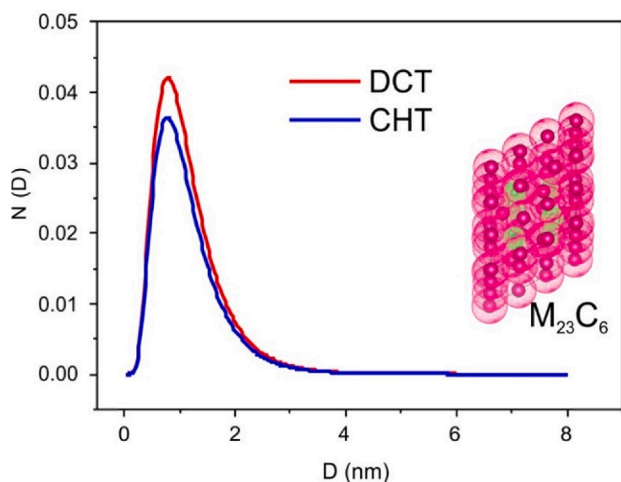


Fig. 4. Particle size (diameter  $D$ ) distribution diagrams for both CHT and DCT samples extracted from the SANS measurements on their states after tempering. The inset depicts the structure of a unit cell of the  $M_{23}C_6$  carbide that is considered to be stable in such a small size range.

extracted distribution diagrams from SANS measurements. These show that there is a large number of scattering features of  $\approx 1\text{--}4$  nm diameter in both the CHT and the DCT sample. These are assumed to be nanoscopic  $M_{23}C_6$  carbides, due to their structural similarity to the Fe matrix, as shown in Fig. 4. In correlation with APT results, the SANS data also shows that the DCT sample has a  $\approx 10\%$  higher fraction of nanoscopic carbides. Together, these results clarify that DCT induces an increase in carbide precipitation compared to the CHT samples across both micrometer and nanometer scale ranges.

### 3.3. Surface chemistry difference between CHT and DCT

SPEM was used in order to understand the evolution and behavior of the alloying elements in the formation of carbides. The ex-situ experiments confirm the duality of the  $M_{23}C_6$  carbide evolution between the CHT and DCT samples. This finding is supported by the SPEM elemental maps shown in Fig. 5a (for CHT) and Fig. 5b (for DCT). The maps show that MC and  $M_6C$  carbides are distinguishable by their V and W content. The  $M_{23}C_6$  carbides in the CHT sample are larger and more alloyed, whereas for the DCT samples they are considerably smaller and barely detectable as their size approximates the spatial resolution of the system. It should be noted that the carbides form not only within the martensitic laths, but also in chains along prior austenite grain boundaries with lower alloying content, which is best seen from the CHT sample (S3). This is confirmed also through APT measurements that indicate an alloyed state of grain boundaries between two martensite laths as presented in S3.

The single-point analysis spectra in Fig. 5c-e and S4 present the chemical changes of the larger V-rich MC and W-rich  $M_6C$  carbides after tempering that occur for both CHT and DCT samples. The major difference between the carbides is in the binding state of C1s, which is shifted towards lower values (around 283 eV) in the MC compared to the  $M_6C$  (around 284 eV) [52]. This is considered to be due to the chemical environment of the C in the MC carbide, where direct M–C bonds are observed in the halite structure [52]. In  $M_6C$ , the C is situated within the octahedral interstitial sites of the FCC structure, and so they are less tightly bonded to the individual metal atoms due to its high ligancy [52], thus forming a similar chemical shift as the C situated within the matrix. This also follows the theory that loosely bonded C is independent of the chemical composition of the matrix and non-stoichiometric carbides that represent a chemically indifferent surrounding for the internal level of C [53]. The double peak character of C1s of the MC carbide may represent the formation of the core-shell type of carbide with a  $M_2C$  to MC structure formed due to tempering as reported in previous work [21]. In this regard, it needs to be clear that the MC carbides before tempering have a transitional character of V-enriched  $M_2C$  carbide type related to the modified alloying caused by prior austenitization heat treatment [21]. Interestingly, the MC carbides display a 0.5 eV shift (dashed lines) in the W4f spectra compared to the  $M_6C$  carbides, considered to be a result of the higher V presence in MC.

Despite their small size, single-point SPEM analysis can be used to investigate, the chemical differences in the formed nanoscopic  $M_{23}C_6$  carbides before and after tempering. The spectra of the matrix (which includes nanoscopic  $M_{23}C_6$  carbides) (S5a-d) for both CHT (top) and DCT (bottom) samples reveal that the  $M_{23}C_6$  carbides evolve towards the  $M_6C$  composition, following the slight presence of Mo (S5e) and W (S5f) and generally low presence of V (S5c) after tempering. The V content is in carbides slightly higher in the CHT carbides than the DCT carbides. Also, DCT induces the  $M_{23}C_6$  carbides to form with Mo that was not present beforehand on the same position. It should be noted that the W and Fe binding states have a chemical shift change of around 3.5 eV and 2 eV after tempering, respectively. Based on chemical shifts, the W state is in matrix/metal bound state of  $W^{6+}$ , whereas in the carbide, it is in a  $W^{4+}$  state [54], corresponding to an oxide state of the surface that is removed with tempering. The Fe shift also consistent with an oxide state [55]. As a result of the oxide formation, the Mo signal could be

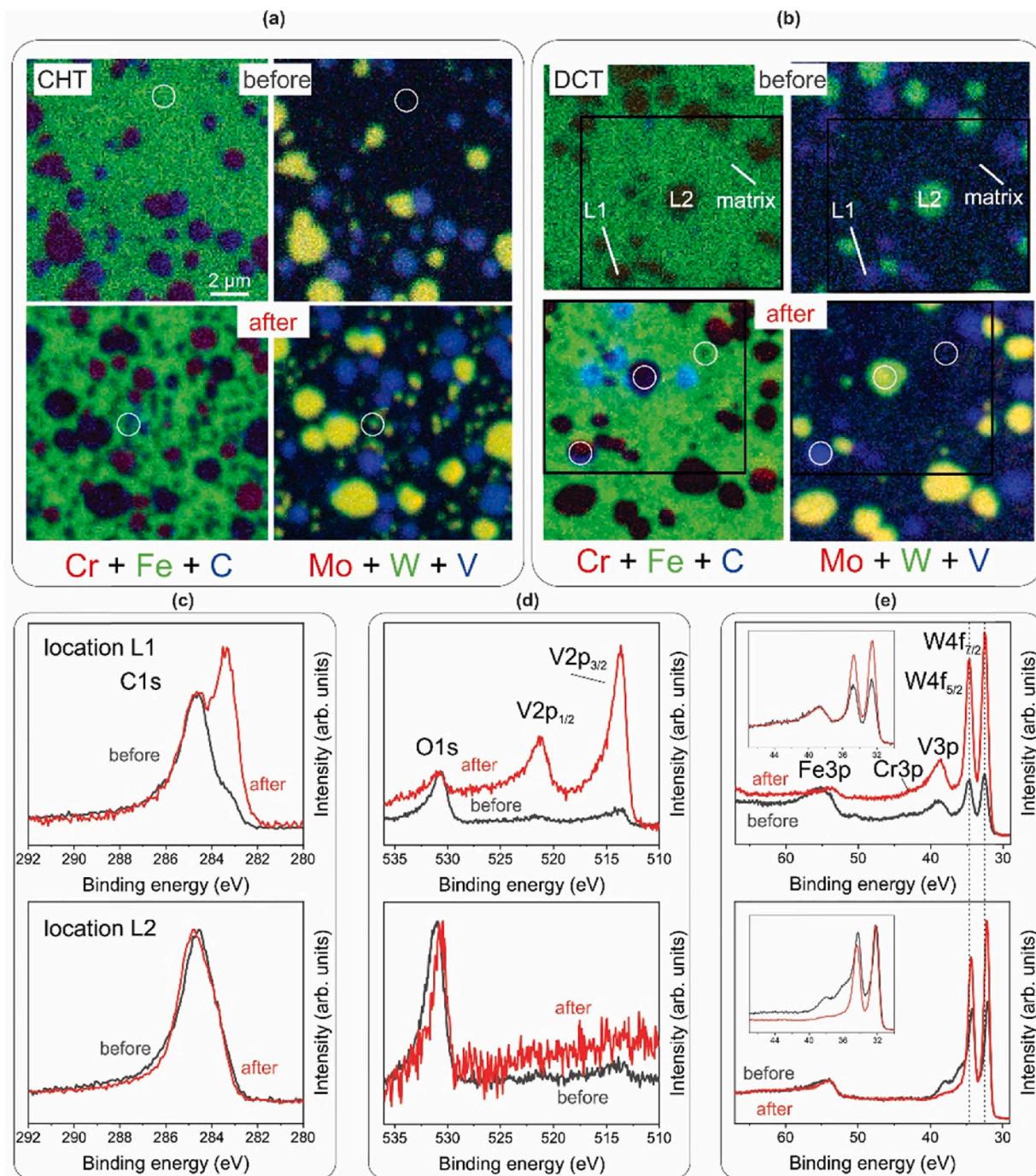


**Fig. 5.** SPEM color-coded elemental maps of selected areas of (a) the CHT and (b) the DCT sample before (top) and after (bottom) tempering. The white circles indicate the exemplar positions probed for point-analysis with XPS. (c)-(e) XPS chemical spectra of the larger MC (top) and  $M_6C$  (bottom) carbides before (dark color) and after (red color) tempering, for (c) C1s (d) V2p and (e) Fe3p, Cr3p, V3p and W4f. The data represents the chemical state of both carbide types for both CHT and DCT samples.

potentially obscured from detection through XPS before tempering, which is consistent with the lower contrast in the color-coded maps of DCT sample before tempering, presented in Fig. 5b.

In both samples, Cr content of this HAFA results in  $M_{23}C_6$  formation during tempering. A comparison between sample types confirms the higher content of Cr and V in CHT carbides compared with the DCT ones when normalized to the Fe3p peak, supporting the APT results presented in S5e-f. The W4f also changes after tempering, showing a + 0.3 eV shift for the DCT  $M_{23}C_6$  carbides compared to the CHT ones. This is again considered to be related to the influence of the slight V alloying of the  $M_{23}C_6$  carbides with CHT, since the chemical shift of the W in the  $M_{23}C_6$

carbides is similar to that of the  $M_6C$  carbides (compare Fig. 5e to S5d). Furthermore, the separation distance between the two W peaks also changes by about 0.1 eV and the width of the peaks is broader for the DCT carbides. This may indicate another chemical state of W, which was not characterized yet in the manuscript.

#### 3.4. In-situ surface chemistry during deep cryogenic treatment

The underlying mechanism of the C redistribution and chemical state changes of the different alloying elements is revealed using in-situ SPEM. Fig. 6a shows smaller carbides formed in the DCT sample

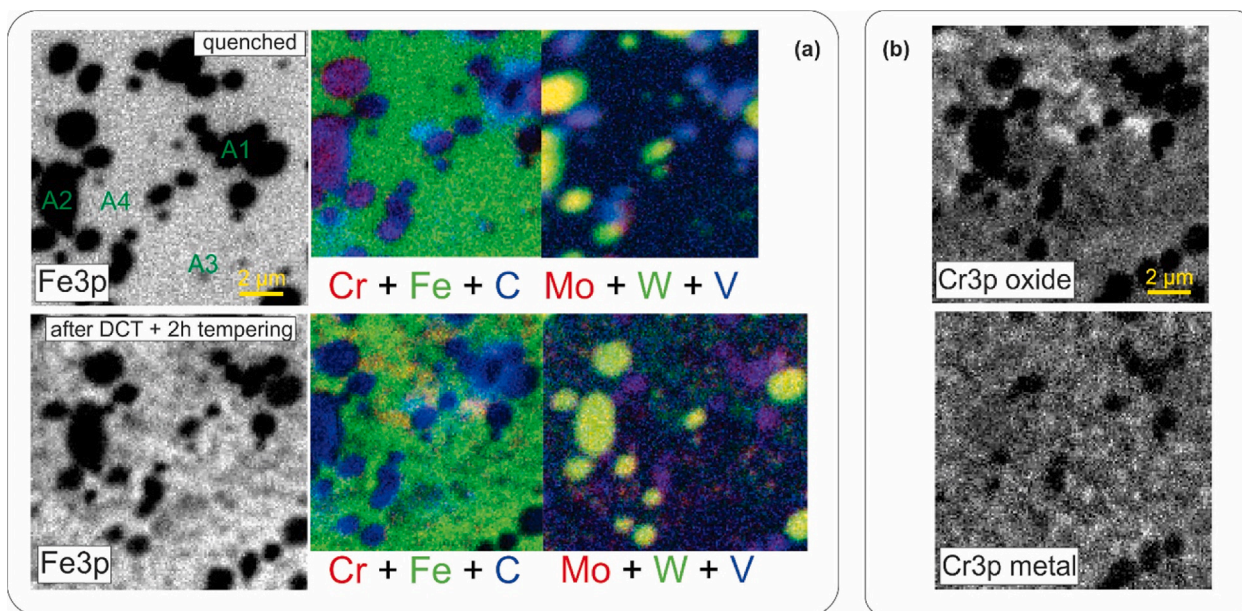


**Fig. 6.** (a) Greyscale Fe3p maps and SPEM color-coded elemental maps after quenching (before tempering and DCT) and after tempering with prior DCT. (b) Cr 3p<sub>2/3</sub> maps with separated signal presentation of the Cr-O shift (above) and metal-metal shift (below).

following tempering. These smaller carbides are now visible as the tempering removed some surface oxide. The chemical maps also show a slight contrast gradient in the matrix after tempering (best seen from the Mo + W + V map gradient from dark blue/purple to dark green across the frame of the image). This gradient occurs due to the slight oxidation formed during the sample transfer from the cooling stage to heating stage for the in-situ measurements, which is performed in ambient environment. However, this does not impair the development of the carbides nor does it influence the surface to disrupt the SPEM analysis. Fig. 6b illustrates this by showing the Cr3p peak associated with oxide and metal, showing negligible Cr oxide formation [56]. Through the deconvolution of the metallic portion and oxide portion, the non-uniform oxidation is revealed and separated from the metallic peak, thus revealing only the newly formed Cr-enriched M<sub>23</sub>C<sub>6</sub> carbides. [56].

Through the deconvolution of the metallic portion and oxide portion, the non-uniform oxidation is revealed and separated from the metallic peak, thus revealing only the newly formed Cr-enriched M<sub>23</sub>C<sub>6</sub> carbides. In-situ measurements were performed during the DCT cooling process, meaning the distribution and binding state for all elements could be traced. It was found that only C displays a change in spatial distribution during the cooling step (example C map before and after 24 h cooling in Fig. 7). The changes are illustrated by subtracting the initial state with the 24 h cooled state as depicted in Fig. 7. With this representation, the changes also need to be carefully considered in relation to the

adventitious C re-deposition artifacts caused by the initial SPEM measurements. In Fig. 7, the artifact is the circular-shaped C enrichment formed over the position A1 (marked in Fig. 6a) caused by the initial high-energy exposure of the X-ray irradiation. With adjustment of the acquisition parameters, subsequent measurements did not result in C contamination. The remaining changes (exemplar features marked with green circles in Fig. 7) are directly related to the segregation of C with prolonged exposure to the cryogenic environment that serve as nucleation points for the later M<sub>23</sub>C<sub>6</sub> carbides. To confirm this, the marked features are correlated with the Fe maps before and after tempering, which confirm that carbides do form on the C-enriched positions (Fig. 7, Fe3p SPEM maps after and before tempering), which were not present in the initial quenched state. These results confirm that the C segregation is effectively visible in the several hundred nanometer resolution, which has up to now has not been reported previously.

Single-point analysis of the C evolution in the vicinity of the pre-existing carbides and within the matrix also reveal that the C does not change binding states during DCT cooling (Fig. 8a-d) and only changes after the carbides are formed during tempering (see in Fig. 8d). This indicates that the carbide-bound states are not modified with DCT cooling, but only their distribution within the metallic matrix is altered. Nevertheless, a change in binding state is determined for Mo, which presents a slight shift of around 0.1–0.2 eV during DCT for all probed positions (Fig. 8a-d). Surprisingly, the intensity ratio between the 3/2

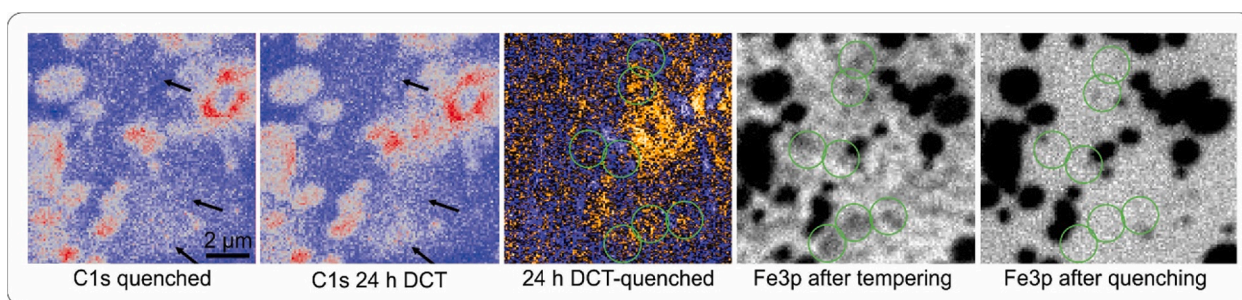


**Fig. 7.** In-situ color-coded C1s concentration maps during entire DCT procedure. The green colored circular markings in the middle image are correlated with the positions on the Fe3p maps after quenching, 24 h DCT cooling and after tempering. The 24 h DCT-quenched image depicts with orange coloration the changes in C signal from the quenched state to the 24 h DCT cooled state.

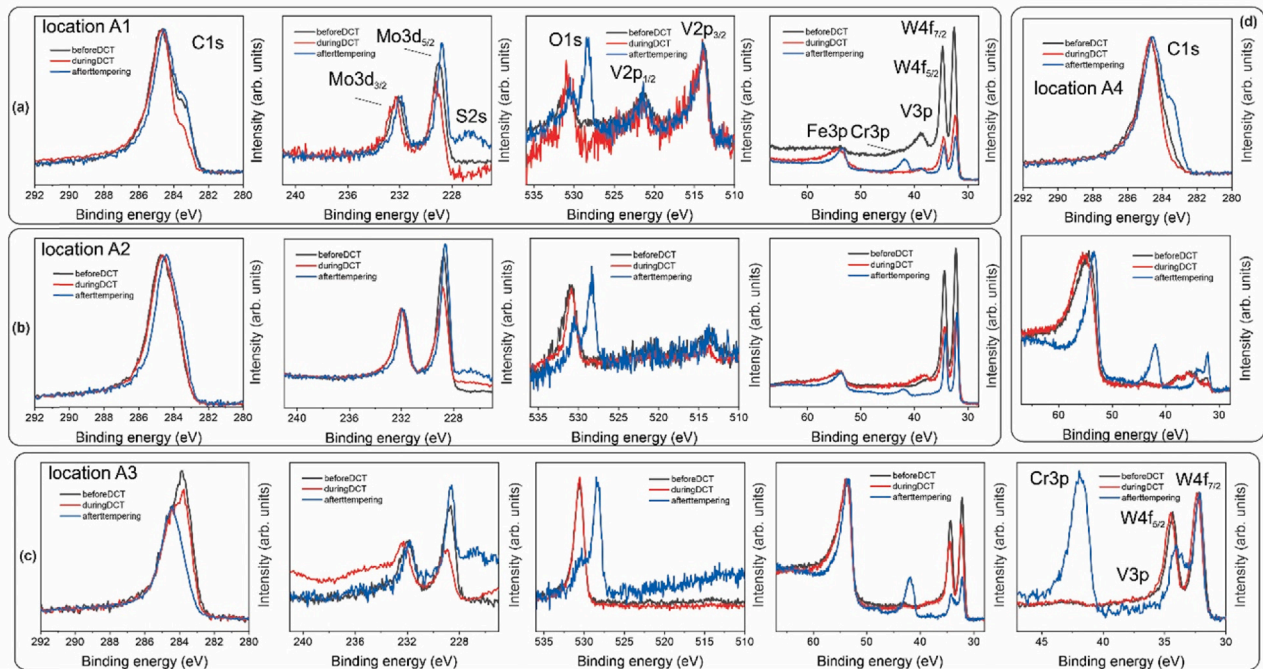


**Fig. 8.** (a–d) XPS chemical spectra of the different positions on the in-situ DCT sample, marked in Fig. 7, before DCT (dark color), during DCT (red color) and after tempering (blue color) for (left to right) C1s, Mo3d, V2p and Fe3p, Cr3p, V3p, W4f.

and 5/2 Mo3d peaks changes that display a lower 5/2 intensity of about 30–50 %, when normalizing to the 3/2 peak. A possible explanation lies in the transition of the  $\text{Mo}^{3+}$  state to a  $\text{Mo}^{4+}$  state. The reasoning for such a transition will be discussed further in the next section. This feature illustrates the effect of DCT on the bonding state of Mo, which uniquely impacts only this alloying element as the other elements do not display any changes during DCT (Fig. 8). This phenomenon is specifically visible around smaller prior  $\text{M}_6\text{C}$  carbides and matrix (location A3, Fig. 8c) that display the strongest modifications of the Mo peaks as well as the additional presence of higher charged states of Mo during DCT. A line scan of the Mo spectra across a carbide and surrounding matrix before DCT and after DCT was performed. The line scan clearly shows the shift changes bound to the matrix and not carbide itself with exposure to DCT (S6). Notably, after warming the sample to room temperature, the Mo peak shifts and new ratios remain similar. Only after the tempering does the Mo return to a binding state similar to what it was before DCT. This suggests that the modified state of Mo is a metastable transition state, which is relaxed through input of the thermal energy and precipitation and growth of carbides.

In response to the tempering procedure and Mo modifications, the W binding in the matrix (locations A3 and A4, Fig. 8c–d) is changed in a dissimilar fashion compared to the states found in CHT sample (S5d). Both probed locations display a stronger asymmetry between the  $\text{W}4f_{7/2}$  and  $\text{W}4f_{5/2}$  peaks, at which the latter displays a halved relative intensity in comparison to the state before. This interesting feature cannot be associated to the presence of the Cr enrichment caused by the formation of the  $\text{M}_{23}\text{C}_6$  carbides as similar enrichment does not form such changes in the CHT sample. It is proposed that Mo plays a crucial role in the different carbide precipitation following DCT. It is also clear that this feature is related only to the formation of the  $\text{M}_{23}\text{C}_6$  carbides in the matrix, since the W binding state remains similar around the  $\text{M}_6\text{C}$  and MC carbides (location A1 and A2, Fig. 8a–b). Additionally, a shift of  $\approx 0.6$  eV shift towards lower energies is observed for the  $\text{W}4f_{5/2}$  peak suggesting preferential carbide build-up with specific incorporation of W in a tighter form, such as  $\text{W}_2\text{C}$  [57]. These are consistent with the ex-situ measurement of the change of W binding state following DCT that was partially obscured by the oxidized matrix.

### 3.5. Theoretical evaluation of C and Mo modification with DCT

The C segregation and change in Mo binding state are key to understanding how DCT affects the precipitation modification of this HAFA. From the microstructural evaluation as well as previous studies [21] the amount of precipitation is significantly higher with DCT, yielding significantly higher volume fraction of  $\text{M}_{23}\text{C}_6$  carbides than what is expected from thermodynamic calculations [21]. This is consistent with the improvement of some mechanical properties of this HAFA as reported previously [58].

Based on our results, we propose that the mechanism is related to the primordial formation of  $\text{M}_2\text{C}$ -like agglomerates that provide a lower energy barrier for the  $\text{M}_7\text{C}_3$  carbides to form, and that these later develop into  $\text{M}_{23}\text{C}_6$  carbides. The proposed mechanism and individual phenomena are sketched in Fig. 9a–c. The SPEM results show that, during DCT the C atoms agglomerate at specific locations, forming C-enriched area. This is consistent with the proposed theories of cryogenically-activated C-capture through gliding dislocations and dislocation recombination [22]. The dislocations meet at specific defects and boundaries that act as sinks for the captured C atoms. Up to now, most researchers postulated that only the C atoms play the main role in the increasing the rate of precipitation. However, this is inconsistent with individual HAFA that do not deliver increased precipitation [21,39]. In our previous study we have confirmed that HAFAs with low Mo and W alloying [39] do not form higher volume of  $\text{M}_{23}\text{C}_6$  carbides, which was attributed due to the deterred carbide nucleation caused by the high W content, and formation of larger  $\text{M}_6\text{C}$  carbides.

However, with the SPEM measurements we can expand this explanation to include the effect of Mo on  $\text{M}_7\text{C}_3$  nucleation. We propose that during the agglomeration of the C on specific sites, the C is further attracted towards Mo rather than other alloying elements (Fig. 9a, from step 1 to step 2 as marked on the figure) caused by the lowest energy state of  $\text{M}_2\text{C}$  carbides [59–61]. In response to this, the C and Mo form pre-existing agglomerations/embryos for the precipitation of the next stage of carbides, that can form more effectively and in a densely during tempering. As a result, the embryos rapidly transition to many  $\text{Mo}_2\text{C}$  carbides, which can immediately transform into  $\text{M}_7\text{C}_3$ . This leads to a

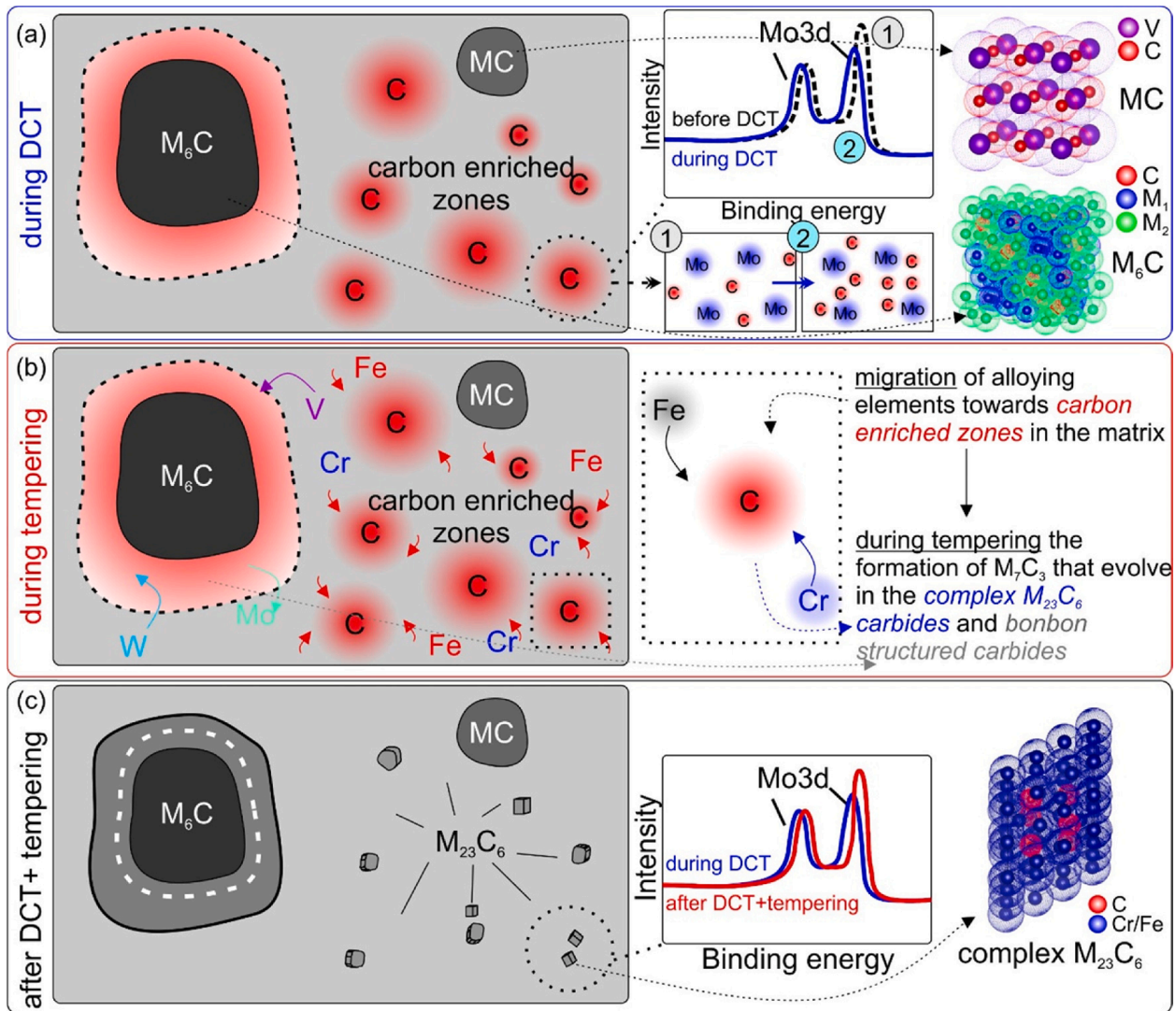


Fig. 9. The schematic representation of carbide evolution and surface chemistry changes during DCT in combination with Mo.

large increase in the precipitation and growth of carbides. At increased temperatures there is an increase in the mobility of alloying elements towards newly carbides  $M_7C_3$  during warming up and tempering (Fig. 9b). This accelerates the overall reaction sequence, as shown in (Fig. 10). This explains why DCT enables high volumetric fractions of  $M_{23}C_6$ , at quantities that would normally require more than 10 h of tempering in a CHT sample.

Due to the increased precipitation density, depletion of alloying elements and morphological reformation of carbides also occurs during tempering. In response to this, the Cr enrichment for the  $M_{23}C_6$  carbides with DCT is lower as the transition from  $M_7C_3$  is faster and bound to a smaller prior carbide volume (Fig. 9b).

In DCT samples, the remaining alloying elements (W, Mo and V), are also diverted toward the preexisting large carbides, which form an enriched shell (see Fig. 9c). This results in a lower concentration of W, Mo and V in  $M_{23}C_6$  DCT carbides compared to the CHT ones. Due to the thermal activation of the alloying elements, the binding state of these elements is also changed (Fig. 9c). Not all of the carbides have equal transformation kinetics, leading to residual  $M_7C_3$  carbides for both CHT and DCT. As a result of the shorter tempering time for DCT, the  $M_7C_3$  carbides have a higher Mo content in comparison to the CHT ones, as displayed by the APT results. This is consistent with the proposed model with prior Mo-enriched  $M_2C$  carbides acting as nuclei for the  $M_7C_3$  carbides. With the above proposed theoretical assessment and chemical

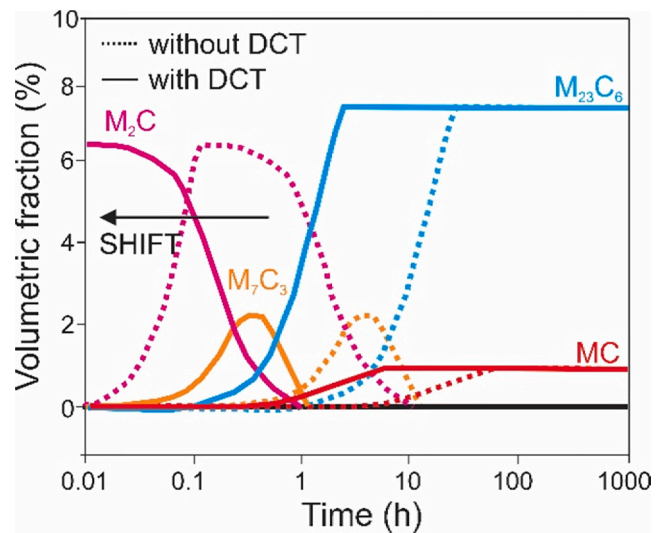


Fig. 10. The graph represents the theoretically modelled precipitation of main carbide types in the high-alloyed ferrous alloy, with and without DCT. The application of DCT causes the shift in the time of precipitation towards earlier stages of the order of the precipitation.

as well as microstructural results, we provide the first holistic model of the influence of DCT on HAFA and also the first theoretical justification for its varying effectiveness on different HAFA and their properties that is instigated by the alloying composition and its atomistic effect on the primordial carbide formation. Furthermore, this study provided the means to explain the chemical and microstructure origin of modified properties (mechanical properties [6,42,58], corrosion properties [62–65], surface properties [28] and wear properties [66–69]) of HAFA with DCT.

#### 4. Conclusion

By using APT, SANS and SPEM, we have studied the effect of DCT on the formation of carbides in HAFA, specifically the segregation and agglomeration of carbon and the alloying elements. This study confirms the following:

1. DCT increases carbide precipitation (by at least 18 vol%) on both micrometer and nanometer scale. DCT promotes a higher density of sub-micrometer  $M_{23}C_6$  and  $M_7C_3$  carbides, and modifies their structure.
2. The APT data provides the first near-atomic scale confirmation of the effect of DCT on the mobility of alloying elements during tempering and the preferential formation of  $M_7C_3$  carbides with Mo enrichment. With DCT, the nanoscopic  $M_{23}C_6$  carbides develop with lower Cr, V and Mo alloying content, but with a core-shell structure with an enriched Cr-shell.
3. SPEM reveals that DCT does not alter the chemical binding state of C. However, it changes the binding state of Mo towards higher charge state (from  $Mo^{3+}$  to  $Mo^{4+}$ ).
4. With exposure of HAFA to cryogenic temperatures, the C is agglomerated into regions around 100 nm diameter. The change in C and Mo are associated with the development of loosely-formed primordial  $M_2C$  carbides that act as nucleation points for next generation carbides.
5. The Mo modification with DCT leads to enhanced formation of Mo-enriched  $M_7C_3$  carbides. The modified  $M_7C_3$  carbides are thermodynamically associated with a separate  $M_7C_3$  sub-type that is theoretically feasible at cryogenic temperatures. The increased population of  $M_7C_3$  carbides results in a significant increase in  $M_{23}C_6$  carbide nucleation and precipitation, thus reaching the maximum number of carbides in shorter tempering times.
6. The Mo activation with DCT provides a meaningful mechanism for the diverse influence of DCT on the precipitation dynamics of differently alloyed HAFA and provides the first consistently applicable explanation for the improved precipitation kinetics.

#### CRedit authorship contribution statement

**Patricia Jovičević-Klug:** Conceptualization, Methodology, Investigation, Visualization, Writing – original draft, Writing – review & editing. **Levi Tegg:** Methodology, Investigation, Visualization, Writing – original draft, Writing – review & editing. **Matic Jovičević-Klug:** Conceptualization, Methodology, Investigation, Visualization, Writing – original draft, Writing – review & editing. **Rahul Parmar:** Methodology, Writing – review & editing. **Matteo Amati:** Methodology, Writing – review & editing. **Luca Gregoratti:** Methodology, Writing – review & editing. **László Almásy:** Supervision, Resources, Writing – review & editing. **Julie M. Cairney:** Supervision, Resources, Writing – review & editing. **Bojan Podgornik:** Supervision, Resources, Writing – review & editing.

#### Declaration of Competing Interest

The authors declare that they have no known competing financial interests or personal relationships that could have appeared to influence

the work reported in this paper.

#### Data availability

Data will be made available on request.

#### Acknowledgment

The authors acknowledge the technical and scientific assistance of Institute of Metals and Technology, Slovenia, Elettra Sincrotrone Trieste, Italy and Sydney Microscopy & Microanalysis, the University of Sydney node of Microscopy Australia.

#### Appendix A. Supplementary material

S1: Additional SEM micrographs of sample tips following atom probe tomography analysis.

S2: Additional 3D video model of tested samples.

S3: Profile chemical analysis of a martensite-martensite grain boundary with APT.

S4: Additional XPS chemical spectra of carbides before and after tempering for Mo3d.

S5: Additional XPS chemical spectra of the matrix material of CHT and DCT samples before and after tempering.

S6: Line scan of carbide before DCT and during DCT.

Supplementary data to this article can be found online at <https://doi.org/10.1016/j.apsusc.2022.155497>.

#### References

- [1] P. Baldissera, C. Delprete, Deep Cryogenic Treatment: A Bibliographic Review, The Open Mechanical Engineering Journal 2 (2008) 1–11, <https://doi.org/10.2174/1874155X00802010001>.
- [2] D. Senthilkumar, Cryogenic Treatment: Shallow and Deep, in: G.E. Totten, R. Colas (Eds.), Encyclopedia of Iron, Steel, and Their Alloys, Taylor and Francis: NY, USA, New York, NY, 2016: pp. 995–1007. <https://doi.org/10.1081/E-EISA-120052805>.
- [3] L. Tóth, Examination of the properties and structure of tool steel en. 1. 2379 due to different heat treatments, 3 (2018) 1–7.
- [4] N.A. Özbek, A. Cicek, M. Gülesin, Ö. Özbek, P. Chen, T. Malone, P. Torres, R. Bond, O. Senkov, S. Senkova, A.L. Woodcraft, W.S. Lee, C.R. Lin, D.H. Park, S.W. Choi, J. H. Kim, J.M. Lee, M. Kumar, N. Sotirov, F. Grabner, R. Schneider, G. Mozdren, S. Budurov, S. Yaneva, N. Stoichev, P. van Bá, Y.B. Lee, D.H. Shin, K.T. Park, W.J. Nam, A. Molinari, I. Lonardelli, K. Demetrio, C. Menapace, V.F. Steier, E.S. Ashiuchi, Reissig, L., J.A. Araujo, M. Levine, C. White, Y.T. Lin, M.C. Wang, Y. Zhang, Y.Z. He, D.P. Wang, Y. Wang, Z. Jiang, O. Senkov, S. Senkova, Cryogenic mechanical behavior of 5000- and 6000-series aluminum alloys: Issues on application to offshore plants, Cryogenics (Guildf). 146 (2004) 44–58. <https://doi.org/10.1007/1-4020-2112-7>.
- [5] P. v Krot, S. Bobyr, N. v Biba, Modeling of Phase Transformations in the rolls of the special alloy steels during quenching and deep cryogenic treatment modeling of phase transformations in the rolls of the special alloy steels during quenching and deep, (2016).
- [6] A. Molinari, M. Pellizzari, S. Gialanella, G. Straffellini, K.H. Stiasny, Effect of deep cryogenic treatment on the mechanical properties of tool steels, J Mater Process Technol. 118 (2001) 350–355, [https://doi.org/10.1016/S0924-0136\(01\)00973-6](https://doi.org/10.1016/S0924-0136(01)00973-6).
- [7] P. Jovičević-Klug, B. Podgornik, Review on the Effect of Deep Cryogenic Treatment of Metallic Materials in Automotive Applications, Metals (Basel). 10 (2020) 434, <https://doi.org/10.3390/met10040434>.
- [8] M. Jovicvic-Klug, P. Jovicvic-Klug, J. McCord, B. Podgornik, Investigation of microstructural attributes of steel surfaces through magneto-optical Kerr effect, J. Mater. Res. Technol. 11 (2021) 1245–1259, <https://doi.org/10.1016/J.JMRT.2021.01.106>.
- [9] P. Jovičević-Klug, T. Kranjec, M. Jovičević-Klug, T. Kosec, B. Podgornik, Influence of the Deep Cryogenic Treatment on AISI 52100 and AISI D3 Steel's Corrosion Resistance, Materials 2021, Vol. 14, Page 6357. 14 (2021) 6357. <https://doi.org/10.3390/MA14216357>.
- [10] M. Jovicvic-Klug, P. Jovicvic-Klug, T. Kranjec, B. Podgornik, Cross-effect of Surface Finishing and Deep Cryogenic Treatment on Corrosion Resistance of AISI M35 steel, Journal of Materials Research and Technology. 14 (2021) 2365–2381. <https://doi.org/doi.org/10.1016/j.jmrt.2021.07.134>.
- [11] J.W. Kim, J.A. Griggs, J.D. Regan, R.A. Ellis, Z. Cai, Effect of cryogenic treatment on nickel-titanium endodontic instruments, Int Endod J. 38 (2005) 364–371, <https://doi.org/10.1111/j.1365-2591.2005.00945.x>.
- [12] P. Biswas, S. Ghosh, A. Sarkar, N.G. Roy, Investigation of deep cryogenic treatment of Steels for medical tooling applications, J Phys Conf Ser. 1797 (2021), 012057, <https://doi.org/10.1088/1742-6596/1797/1/012057>.

- [13] Industrial Robot: An International Journal. 34 (2007), <https://doi.org/10.1108/IR.2007.04934DAD.002>.
- [14] E. Bartolomé, B. Bozzo, P. Sevilla, O. Martínez-Pasarell, T. Puig, X. Granados, ABS 3D printed solutions for cryogenic applications, *Cryogenics (Guildf)*. 82 (2017) 30–37, <https://doi.org/10.1016/j.cryogenics.2017.01.005>.
- [15] P. Jurčič, M. Dománková, J. Ptačinová, M. Pašák, M. Kusý, P. Priknerová, Investigation of the Microstructural Changes and Hardness Variations of Sub-Zero Treated Cr-V Ledeburitic Tool Steel Due to the Tempering Treatment, *J Mater Eng Perform*. 27 (2018) 1514–1529, <https://doi.org/10.1007/s11665-018-3261-6>.
- [16] K. Prudhvi, V.V. Lakshmi, Cryogenic Tool Treatment, *Imperial Journal of Interdisciplinary Research*. 2 (2016) 1204–1211.
- [17] S. Kalia, Cryogenic processing: A study of materials at low temperatures, *J Low Temp Phys*. 158 (2010) 934–945, <https://doi.org/10.1007/s10909-009-0058-x>.
- [18] M. Villa, M.A.J. Somers, Cryogenic Treatment of Steel : From Concept to Metallurgical Understanding, Proceedings of the 24th International Feratation for Heat Treatment and Surface Engineering Congress. (2017).
- [19] C.J. Ming, Cryogenic Treatment of Music Wire, National University of Singapore, 2004.
- [20] F. Meng, K. Tagashira, H. Sohma, Wear resistance and microstructure of cryogenic treated Fe-1.4Cr-1C bearing steel, *Scr. Metall. Mater.* 31 (1994) 865–868.
- [21] P. Jovičević-Klug, M. Jovičević-Klug, B. Podgornik, Effectiveness of deep cryogenic treatment on carbide precipitation, *J. Mater. Res. Technol.* 9 (2020) 13014–13026, <https://doi.org/10.1016/j.jmrt.2020.09.063>.
- [22] V.G. Gavriljuk, W. Theisen, V. v. Sirosh, E. v. Polshin, A. Kortmann, G.S. Mogilny, Y.N. Petrov, Y. v. Tarusin, Low-temperature martensitic transformation in tool steels in relation to their deep cryogenic treatment, *Acta Mater.* 61 (2013) 1705–1715, <https://doi.org/10.1016/j.actamat.2012.11.045>.
- [23] A. Jaswin, M.L. Dhasan, Effect of Cryogenic Treatment on Corrosion Resistance and Thermal Expansion of Valve Steels, *International Journal of Engineering Technology, Management and Applied Sciences*. 3 (2015) 2349–4476.
- [24] K.E. Moore, N.N. Collins, Cryogenic Treatment of Three Heat Treated Tool Steels, *Key Eng Mater.* 86–87 (1993) 47–54, <https://doi.org/10.5860/CHOICE.33-5121>.
- [25] D.N. Collins, J. Dormer, Deep cryogenic treatment of a D2 cold-work tool steel, *Heat Treat. Met.* 3 (1997) 71–74.
- [26] P. Jovičević-Klug, M. Jovičević-Klug, T. Sever, D. Feizpour, B. Podgornik, Impact of Steel Type, Composition and Heat Treatment Parameters on Effectiveness of Deep Cryogenic Treatment, *Journal of Materials Research and Technology*. 14 (2021) 1007–1020.
- [27] M. Villa, M.A.J. Somers, Cryogenic treatment of an AISI D2 steel: The role of isothermal martensite formation and “martensite conditioning”, *Cryogenics (Guildf)*. 110 (2020), 103131 <https://doi.org/10.1016/j.cryogenics.2020.103131>.
- [28] P. Jovičević-Klug, M. Jenko, M. Jovičević-Klug, B. Šetina Batič, J. Kovač, B. Podgornik, Effect of Deep Cryogenic Treatment on Surface Chemistry and Microstructure of Selected High-Speed Steels, *Appl Surf Sci.* 548 (2021) 1–11.
- [29] J.Y. Huang, Y.T. Zhu, X.Z. Liao, L.J. Beyerlein, M.A. Bourke, T.E. Mitchell, Microstructure of cryogenic treated M2 tool steel, *Mater. Sci. Eng., A*. 339 (2003) 241–244, [https://doi.org/10.1016/S0921-5093\(02\)00165-X](https://doi.org/10.1016/S0921-5093(02)00165-X).
- [30] P. Jovičević-Klug, M. Jovičević-Klug, B. Podgornik, Unravelling the Role of Nitrogen in Surface Chemistry and Oxidation Evolution of Deep Cryogenic Treated High-Alloyed Ferrous Alloy, *Coatings*. 12 (2022) 213, <https://doi.org/10.3390/COATINGS12020213>.
- [31] B.K. Anil Kumar, M.G. Ananthaprasad, K. Gopalakrishna, Action of Cryogenic chill on Mechanical properties of Nickel alloy Metal Matrix Composites, in: International Conference on Advances in Materials and Manufacturing Applications, Bangalore, India, 2016: pp. 1–11. <https://doi.org/10.1088/1757-899X/149/1/012116>.
- [32] D.N. Collins, Deep cryogenic treatment of tool steels: A review, *Heat Treat. Met.* 23 (2010) 40–42, <https://doi.org/10.1080/10426911003720862>.
- [33] A. Antony, N.M. Schmel, A. Sokolova, R. Mahjoub, D. Fabijanic, N.E. Stanford, Quantification of the Dislocation Density, Size, and Volume Fraction of Precipitates in Deep Cryogenically Treated Martensitic Steels, *Metals* 2020, Vol. 10, Page 1561. 10 (2020) 1561. <https://doi.org/10.3390/MET10111561>.
- [34] A. Akhbarizadeh, A. Shafyei, M.A. Golozar, Effects of cryogenic treatment on wear behavior of D6 tool steel, *Mater Des.* 30 (2009) 3259–3264, <https://doi.org/10.1016/j.matdes.2008.11.016>.
- [35] D. Senthilkumar, Effect of deep cryogenic treatment on residual stress and mechanical behaviour of induction hardened En 8 steel, *Advances in Materials and Processing Technologies*. 2 (2016) 427–436, <https://doi.org/10.1080/2374068X.2016.1244326>.
- [36] M. Pellizzari, Influence of deep cryogenic treatment on the properties of conventional and PM high speed steels, *Metallurgia Italiana*. 100 (2008) 17–22.
- [37] M. Pellizzari, D. Caliskanoglu, A. Fernández, J.I. Barbero, B. Pena, T. Uemit, R. Pizarro Sanz, R. Elvira Eguizabal, L.A. Alava, Influence of different deep cryogenic treatment routes on the properties of high speed steel, *HTM Journal of Heat Treatment and Materials*. 67 (2012) 111–117.
- [38] A. Idayan, A. Gnanavelbabu, K. Rajkumar, Influence of Deep Cryogenic Treatment on the Mechanical Properties of AISI 440C Bearing Steel, *Procedia Eng, Elsevier Ltd, in*, 2014, pp. 1683–1691.
- [39] P. Jovičević-Klug, A.Z. Guštin, M. Jovičević-Klug, B. Šetina Batič, A. Lebar, B. Podgornik, Coupled role of alloying and manufacturing on deep cryogenic treatment performance on high-alloyed ferrous alloys, *J. Mater. Res. Technol.* 18 (2022) 3184–3197, <https://doi.org/10.1016/J.JMRT.2022.04.025>.
- [40] F.J. da Silva, S.D. Franco, A.R. Machado, E.O. Ezugwu, A.M. Souza, Performance of cryogenically treated HSS tools, *Wear* 261 (2006) 674–685, <https://doi.org/10.1016/j.wear.2006.01.017>.
- [41] C.L. Gogte, D.R. Peshwe, R.K. Paretkar, Influence of cobalt on the cryogenically treated W-Mo-V high speed steel, in: *Adv Cryog Eng*, Spokane, WA, USA, 2012: pp. 1175–1182. <https://doi.org/10.1063/1.4707039>.
- [42] M. Pellizzari, A. Molinari, L. Girardini, L. Maldarelli, Deep cryogenic treatment of AISI M2 high-speed steel, *Int. J. Microstruct. Mater. Prop.* 3 (2008) 383–390, <https://doi.org/10.1504/IJMMP.2008.018742>.
- [43] P. Jovičević-Klug, B. Podgornik, Comparative study of conventional and deep cryogenic treatment of AISI M3:2 (EN 1.3395) high-speed steel, *Journal of Materials Research and Technology*. 9 (2020) 13118–13127. <https://doi.org/10.1016/j.jmrt.2020.09.071>.
- [44] N.B. Dhokey, A. Hake, S. Kadu, I. Bhoskar, G.K. Dey, Influence of cryoprocessing on mechanism of carbide development in cobalt-bearing high-speed steel (M35), *Metall Mater Trans A Phys Metall Mater Sci.* 45 (2014) 1508–1516, <https://doi.org/10.1007/s11661-013-2067-2>.
- [45] L. Gregoratti, M. Marsi, G. Cautero, M. Kiskinova, G.R. Morrison, A.W. Potts, Spectromicroscopy of interfaces with synchrotron radiation: multichannel data acquisition, *Nuclear Instruments and Methods in Physics Research A*. (2001) 884–888.
- [46] P. Jovičević-Klug, N. Lipovšek, M. Jovičević-Klug, B. Podgornik, Optimized preparation of deep cryogenic treated steel and Al-alloy samples for optimal microstructure imaging results, *Mater Today Commun.* 27 (2021), 102211, <https://doi.org/10.1016/j.mtcomm.2021.102211>.
- [47] L. Almásy, New Measurement Control Software on the Yellow Submarine SANS Instrument at the Budapest Neutron Centre, *Journal of Surface Investigation*. 15 (2021) 527–531, <https://doi.org/10.1134/S1027451021030046/FIGURES/2>.
- [48] B. Gault, M.P. Moody, J.M. Cairney, S.P. Ringer, *Atom Probe Microscopy*, Springer New York, New York, NY, 2012. <https://doi.org/10.1007/978-1-4614-3436-8>.
- [49] D.A. Reinhard, T.R. Payne, E.M. Strennen, E. Oltman, B.P. Geiser, G.S. Sobering, J. Mandt, Improved Data Analysis with IVAS 4 and AP Suite, *Microsc. Microanal.* 25 (2019) 302–303, <https://doi.org/10.1017/S1431927619002241>.
- [50] Y.X. Wu, W.W. Sun, X. Gao, M.J. Styles, A. Arlazarov, C.R. Hutchinson, The effect of alloying elements on cementite coarsening during martensite tempering, *Acta Mater.* 183 (2020) 418–437, <https://doi.org/10.1016/J.ACTAMAT.2019.11.040>.
- [51] George.E.Ph.D. Totten, *Steel Heat Treatment, Metallurgi And Technologies*. (2007) 1–1558. <https://doi.org/doi:10.1201/NOF0849384523.ch6>.
- [52] D. v. Suetin, I.R. Shein, A.L. Ivanovskii, Structural, electronic and magnetic properties of r carbides (Fe<sub>3</sub>W<sub>3</sub>C, Fe<sub>6</sub>W<sub>6</sub>C, Co<sub>3</sub>W<sub>3</sub>C and Co<sub>6</sub>W<sub>6</sub>C) from first principles calculations, *Physica B Condens Matter*. 404 (2009) 3544–3549.
- [53] A.I. Gusev, A.A. Rempel, A.J. Magerl, *Disorder and Order in Strongly Nonstoichiometric Compounds*, Springer, New York, NY, USA, 2001.
- [54] L.N. Zhang, Y.Y. Ma, Z.L. Lang, Y.H. Wang, S.U. Khan, G. Yan, H.Q. Tan, H.Y. Zang, Y.G. Li, Ultrafine cable-like WC/W<sub>2</sub>C heterojunction nanowires covered by graphitic carbon towards highly efficient electrocatalytic hydrogen evolution, *J Mater Chem A Mater.* 6 (2018) 15395–15403.
- [55] K. Zhang, M. Broetmann, H. Hofsaess, Sharp transition from ripple patterns to a flat surface for ion beam erosion of Si with simultaneous co-deposition of iron, *AIP Adv.* 2 (2012), 032123.
- [56] L. Gregoratti, A. Barinov, E. Benfatto, G. Cautero, C. Fava, P. Lacovig, D. Lonza, M. Kiskinova, R. Tommasini, S. Mähl, W. Heichler, Channel electron detector for photoemission spectroscopy and microscopy, *Rev. Sci. Instrum.* 75 (2003), <https://doi.org/10.1063/1.1630837>.
- [57] C.C. Tran, Y. Han, M. Garcia-Perez, S. Kaliaguine, Synergistic effect of Mo–W carbides on selective hydrodeoxygenation of guaiacol to oxygen-free aromatic hydrocarbons, *Catal, Sci Technol.* 9 (2019) 1387–1397, <https://doi.org/10.1039/C8CY02184H>.
- [58] P. Jovičević-Klug, G. Puš, M. Jovičević-Klug, B. Žužek, B. Podgornik, Influence of heat treatment parameters on effectiveness of deep cryogenic treatment on properties of high-speed steels, *Mater. Sci. Eng., A*. 829 (2022), 142157, <https://doi.org/10.1016/j.msea.2021.142157>.
- [59] S. Yamasaki, H.K.D.H. Bhadeshia, Modelling and characterisation of Mo<sub>2</sub>C precipitation and cementite dissolution during tempering of Fe–C–Mo martensitic steel, <http://Dx.Doi.Org/10.1179/026708303225002929>. 19 (2013) 723–731. <https://doi.org/10.1179/026708303225002929>.
- [60] Y. Liu, J. Li, W. Liang, J. Gao, Y. Qi, C. Shang, Precipitation Behaviors of Carbides in High Speed Steel during ESR and Heat Treatment, *Metals* 2021, Vol. 11, Page 1781. 11 (2021) 1781. <https://doi.org/10.3390/MET11111781>.
- [61] K.J. Kurzydowski, W. Zieliński, Mo<sub>2</sub>C → M<sub>6</sub>C carbide transformation in low alloy Cr–Mo ferritic steels, <http://Dx.Doi.Org/10.1179/030634584790420195>. 18 (2013) 223–224. <https://doi.org/10.1179/030634584790420195>.
- [62] J. Voglar, Ž. Novak, P. Jovičević-Klug, B. Podgornik, T. Kosec, Effect of Deep Cryogenic Treatment on Corrosion Properties of Various High-Speed Steels, *Metals (Basel)*. 11 (2020) 14, <https://doi.org/10.3390/met11010014>.
- [63] W. Wang, V. Srinivasan, S. Siva, B. Albert, M. Lal, A. Alfantazi, Corrosion behavior of deep cryogenically treated AISI 420 and AISI 52100 steel, *Corrosion*. 70 (2014) 708–720, <https://doi.org/10.5006/1150>.
- [64] S. Ramesh, B. Bhuvaneshwari, G.S. Palani, D.M. Lal, N.R. Iyer, Effects on corrosion resistance of rebar subjected to deep cryogenic treatment, *J. Mech. Sci. Technol.* 31 (2017) 123–132, <https://doi.org/10.1007/s12206-016-1211-5>.
- [65] I. Uygur, H. Gerengi, Y. Arslan, M. Kurtay, The effects of cryogenic treatment on the corrosion of AISI D3 steel, *Mater. Res.* 18 (2015) 569–574, <https://doi.org/10.1590/1516-1439.349914>.
- [66] R. Thornton, T. Slatter, H. Ghadbeigi, Effects of deep cryogenic treatment on the dry sliding wear performance of ferrous alloys, *Wear* 305 (2013) 177–191, <https://doi.org/10.1016/j.wear.2013.06.005>.

- [67] J. Li, X. Yan, X. Liang, H. Guo, D.Y. Li, Influence of different cryogenic treatments on high-temperature wear behavior of M2 steel, *Wear* 376–377 (2017) 1112–1121, <https://doi.org/10.1016/j.wear.2016.11.041>.
- [68] D. Das, A.K. Dutta, K.K. Ray, Sub-zero treatments of AISI D2 steel: Part II, Wear behavior, *Materials Science and Engineering A*. 527 (2010) 2194–2206, <https://doi.org/10.1016/j.msea.2009.10.071>.
- [69] P. Jovičević-Klug, M. Sedláček, M. Jovičević-Klug, B. Podgornik, Effect of Deep Cryogenic Treatment on Wear and Galling Properties of High-Speed Steels, *Materials*. 14 (2021) 1–16, <https://doi.org/10.3390/met11010014>.